

# Jet multiplicity in the proto-binary system NGC1333-IRAS4A

## The detailed CALYPSO IRAM-PdBI view<sup>★</sup>

G. Santangelo<sup>1,2</sup>, C. Codella<sup>1</sup>, S. Cabrit<sup>3,4,5,6</sup>, A. J. Maury<sup>7</sup>, F. Gueth<sup>8</sup>, S. Maret<sup>5,6</sup>, B. Lefloch<sup>5,6</sup>, A. Belloche<sup>9</sup>, Ph. André<sup>7</sup>, P. Hennebelle<sup>7</sup>, S. Anderl<sup>5,6</sup>, L. Podio<sup>1</sup>, and L. Testi<sup>10,1</sup>

<sup>1</sup> Osservatorio Astrofisico di Arcetri, Largo Enrico Fermi 5, I-50125 Florence, Italy

e-mail: gina.santangelo@oa-roma.inaf.it

<sup>2</sup> Osservatorio Astronomico di Roma, via di Frascati 33, 00040 Monteporzio Catone, Italy

<sup>3</sup> LERMA, Observatoire de Paris, PSL Research University, CNRS, UMR 8112, F-75014, Paris France

<sup>4</sup> Sorbonne Universités, UPMC Univ. Paris 6, UMR 8112, LERMA, F-75005, Paris, France

<sup>5</sup> Univ. Grenoble Alpes, IPAG, F-38000 Grenoble, France

<sup>6</sup> CNRS, IPAG, F-38000 Grenoble, France

<sup>7</sup> Laboratoire AIM-Paris-Saclay, CEA/DSM/Irfu – CNRS – Université Paris Diderot, CE-Saclay, 91191 Gif-sur-Yvette, France

<sup>8</sup> IRAM, 300 rue de la Piscine, 38406 Saint Martin d'Hères, France

<sup>9</sup> Max-Planck-Institut für Radioastronomie, Auf dem Hügel 69, 53121 Bonn, Germany

<sup>10</sup> ESO, Karl-Schwarzschild-Strasse 2 D-85748 Garching bei München, Germany

Received April 16, 2015; accepted August 17, 2015

### ABSTRACT

**Context.** Owing to the paucity of sub-arcsecond (sub)mm observations required to probe the innermost regions of newly forming protostars, several fundamental questions are still being debated, such as the existence and coevality of close multiple systems.

**Aims.** We study the physical and chemical properties of the jets and protostellar sources in the NGC1333-IRAS4A proto-binary system using continuum emission and molecular tracers of shocked gas.

**Methods.** We observed NGC1333-IRAS4A in the SiO(6–5), SO(6<sub>5</sub>–5<sub>4</sub>), and CO(2–1) lines and the continuum emission at 1.3, 1.4, and 3 mm using the IRAM Plateau de Bure Interferometer in the framework of the CALYPSO large program.

**Results.** We clearly disentangle for the first time the outflow emission from the two sources A1 and A2. The two protostellar jets have very different properties: the A1 jet is faster, has a short dynamical timescale ( $\lesssim 10^3$  yr), and is associated with H<sub>2</sub> shocked emission, whereas the A2 jet, which dominates the large-scale emission, is associated with diffuse emission, bends, and emits at slower velocities. The observed bending of the A2 jet is consistent with the change of propagation direction observed at large scale and suggests jet precession on very short timescales ( $\sim 200$ – $600$  yr). In addition, a chemically rich spectrum with emission from several complex organic molecules (e.g. HCOOH, CH<sub>3</sub>OCHO, CH<sub>3</sub>OCH<sub>3</sub>) is only detected towards A2. Finally, very high-velocity shocked emission ( $\sim 50$  km s<sup>–1</sup>) is observed along the A1 jet. An LTE analysis shows that SiO, SO, and H<sub>2</sub>CO abundances in the gas phase are enhanced up to  $(3\text{--}4)\times 10^{-7}$ ,  $(1.4\text{--}1.7)\times 10^{-6}$ , and  $(3\text{--}7.9)\times 10^{-7}$ , respectively.

**Conclusions.** The intrinsic different properties of the jets and driving sources in NGC1333-IRAS4A suggest different evolutionary stages for the two protostars, with A1 being younger than A2, in a very early stage of star formation previous to the hot-corino phase.

**Key words.** Stars: formation – Stars: low-mass – ISM: jets and outflows – ISM: individual objects: NGC1333-IRAS4A – ISM: molecules

## 1. Introduction

Although multiple systems are a common outcome of the star formation process, the mechanism for their formation is still being debated (e.g. Tohline 2002; Reipurth et al. 2014, and references therein). In this context, information about the system's multiplicity, coevality, and environment are particularly crucial. The ideal laboratories for these studies are very young sources that have not undergone significant evolution and are thus likely keep a memory of the initial physical and chemical conditions. Class 0 protostars, with lifetimes of less than a few  $10^5$  yr, represent the earliest stage of low-mass star formation, when most of the mass is still in the form of a dense infalling envelope (e.g.

André et al. 2000; Evans et al. 2009). Once it is sufficiently luminous, the central protostar radiatively heats the surrounding inner envelope, and grain mantle evaporation occurs, which triggers a hot-corino chemistry rich in complex organic molecules (COMs) (van Dishoeck & Blake 1998; Ceccarelli 2004; Bottinelli et al. 2004). Protostars also drive fast jets (e.g. Arce et al. 2007; Ray et al. 2007; Frank et al. 2014) that impact the high-density parent cloud and generate shock fronts. This leads to significant enhancements in the abundance of several molecules, such as H<sub>2</sub>O, CH<sub>3</sub>OH, and SiO (e.g. van Dishoeck & Blake 1998). High angular resolution studies of Class 0 protostars are thus needed to probe the innermost regions ( $\leq 100$  AU) with the aim of disentangling the emission originating from the different processes: the launch of the jet, the outflow cavity emission, and the chemistry of the hot corino. We present here new observations of molecular tracers of shocked gas and continuum emission towards the

<sup>★</sup> Based on observations carried out with the IRAM Plateau de Bure Interferometer. IRAM is supported by INSU/CNRS (France), MPG (Germany), and IGN (Spain).

NGC1333-IRAS4A protostellar system (hereafter IRAS4A) located at 235 pc (Hirota et al. 2008). Observations are part of the Continuum and Lines in Young ProtoStellar Objects (CALYPSO)<sup>1</sup> large program, aimed at studying a large sample of Class 0 protostars at sub-arcsecond resolution with the IRAM Plateau de Bure Interferometer (hereafter PdBI).

IRAS4A has been identified as a binary Class 0 system using mm interferometry (Jennings et al. 1987; Sandell et al. 1991; Lay et al. 1995; Looney et al. 2000). Since the binary components have never been resolved in the infrared band, the luminosity of each protostar is not known. The bolometric luminosity of the IRAS4A system has been derived by Enoch et al. (2009) to be  $\sim 4.2 L_{\odot}$  and later by Kristensen et al. (2012) and Karska et al. (2013) to be  $\sim 9.1 L_{\odot}$  using PACS continuum measurements. The two Class 0 components, IRAS4A1 and IRAS4A2 (hereafter A1 and A2), have a separation of only about  $1.8''$  ( $\sim 420$  AU). A1 is more than three times brighter in the millimetre and centimetre continuum than its companion A2 (Looney et al. 2000; Reipurth et al. 2002; Jørgensen et al. 2007), whereas it is weaker in  $\text{NH}_3$  emission (Choi et al. 2007). The IRAS4A system is associated with a spectacular large-scale (a few arcminutes) bipolar outflow (PA  $\sim 45^\circ$ ) observed in several tracers, such as CO, SiO, and  $\text{H}_2\text{O}$  (e.g. Blake et al. 1995; Choi 2001, 2005; Yıldız et al. 2012; Santangelo et al. 2014). A shorter southern monopolar blue-shifted lobe (PA  $\sim -10^\circ$ ) is observed in SiO by Choi (2005) with no clear northern counterpart. However, none of the observations to date resolve the emission within  $\sim 10''$  from the protostars and therefore they do not allow us to disentangle the outflow emission and directly identify the driving sources. In this context, the new high angular resolution observations of CO, SiO, and SO presented here allow us to probe the innermost region of IRAS4A. The goal is to study jet multiplicity and the physical and chemical properties of the jet and the driving sources.

## 2. Observations

IRAS4A was observed at 1.3, 1.4, and 3 mm with the IRAM PdBI between February 2011 and February 2013 using both the A and C configurations. The baseline range of the observations is 15–762 m, which allows us to recover emission on scales from  $18''$  to  $0''.35$  at 1.3 mm. WideX backends were used to cover the full 3.8 GHz spectral window at the spectral resolution of 2 MHz ( $\sim 2.7 \text{ km s}^{-1}$  at 1.4 mm). In addition, higher resolution backends were employed to observe the SiO( $5-4$ ), SO( $6_5-5_4$ ), and CO( $2-1$ ) lines at 217.105, 219.949, and 230.538 GHz. Calibration was carried out following standard procedures, using GILDAS-CLIC<sup>2</sup>. The phase RMS is  $\leq 50^\circ$  and  $\leq 80^\circ$  for the A and C tracks, with precipitable water vapour (PWV) between 0.5 mm and 2 mm and system temperatures between 100 K and 250 K. The uncertainty on the absolute flux scale is  $\sim 10\%$ . The synthesised FWHM beam is  $0''.7 \times 0''.4$  (PA =  $19^\circ$ ) at 1.3 mm,  $1''.1 \times 0''.8$  ( $19^\circ$ ) at 1.4 mm, and  $1''.8 \times 1''.3$  ( $39^\circ$ ) at 3 mm. The typical RMS noise per  $1 \text{ km s}^{-1}$  channel is  $\sim 8 \text{ mJy/beam}$  at 1.3 mm,  $\sim 10 \text{ mJy/beam}$  at 1.4 mm, and  $\sim 3 \text{ mJy/beam}$  at 3 mm.

## 3. Results

### 3.1. Continuum emission: source multiplicity and properties

Emission maps of the 1.3 and 3 mm continuum are shown in Fig. 1. Both known protostars A1 and A2 are detected in the

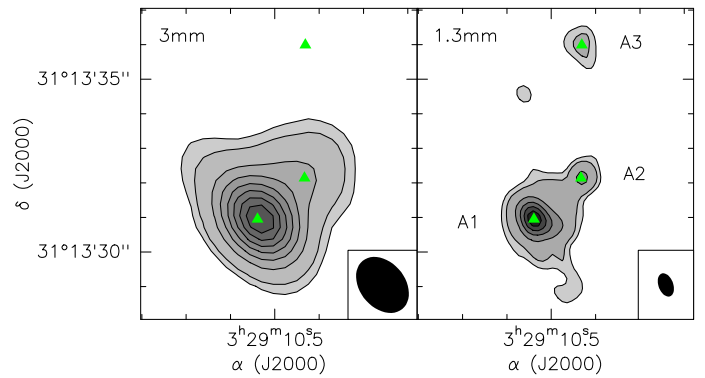


**Fig. 1.** *Left:* 3 mm continuum emission map of the IRAS4A region (grey scale and black contours). The contour levels of emission are traced at 5 and 8  $\sigma$  levels and increase in steps of 10  $\sigma$ , where  $\sigma = 2 \text{ mJy beam}^{-1}$ . The positions of the continuum sources at 1.3 mm are marked in green. The PdBI synthesised beam (HPBW) of the continuum map is shown. *Right:* 1.3 mm continuum map of IRAS4A. Contour levels and labels are the same as in the left panel. The rms noise is  $\sigma = 8 \text{ mJy beam}^{-1}$ .

**Table 1.** Parameters of the continuum peaks.

Source	$\alpha(\text{J2000})$ ( $03^{\text{h}} 29^{\text{m}}$ )	$\delta(\text{J2000})$ ( $31^\circ 13'$ )	Flux <sup>a</sup>	
			1.3mm (mJy)	3mm (mJy)
A1	10 <sup>h</sup> 53	31 <sup>m</sup> 0	1230	144
A2	10 <sup>h</sup> 42	32 <sup>m</sup> 3	369	40
A3	10 <sup>h</sup> 44	35 <sup>m</sup> 9	187	<2

**Notes.** <sup>(a)</sup> Fluxes are measured by integrating over  $1''$ . The uncertainty on the absolute flux is 10%, which translates into an uncertainty of 15% on the spectral indexes (see Sect. 3.1).

continuum emission at all frequencies with A1 being brighter than A2. They are well resolved at 1.3 mm, with a separation of  $\sim 1''.8$ . In addition, a third continuum source (hereafter A3) is detected for the first time only at 1.3 mm at a position ( $+0''.2$ ,  $+3''.7$ ) offset from A2. Positions and integrated fluxes of the three continuum sources are derived by performing a power-law fit to the continuum visibilities of the detected sources (see Table 1).

We estimate the spectral index of the continuum emission  $\alpha_{3 \text{ mm}}^{1.3 \text{ mm}}$  (where flux density is  $F_\nu \propto \nu^\alpha$ ) for the three detected sources. Spectral indexes of 2.3 and 2.4 are obtained for sources A1 and A2, respectively, which are consistent with dust thermal radiation from embedded protostellar objects. On the other hand, the non-detection of source A3 at 1.4 and 3 mm implies a steep spectrum for this source with a spectral index  $\alpha_{3 \text{ mm}}^{1.3 \text{ mm}} > 4.9$  (based on the upper limit on the 3 mm flux density), which is not consistent with a protostellar nature. Compact continuum emission along protostellar jets has already been observed in other sources (e.g. Gueth et al. 2003; Maury et al. 2010; Codella et al. 2014); envelope emission or shock-heated dust along the jet have been suggested as possible explanations for the origin of these features. However, a larger statistically suitable sample is crucial in order to assess this issue. A detailed analysis of the continuum emission in the whole CALYPSO sample will be presented in a forthcoming paper.

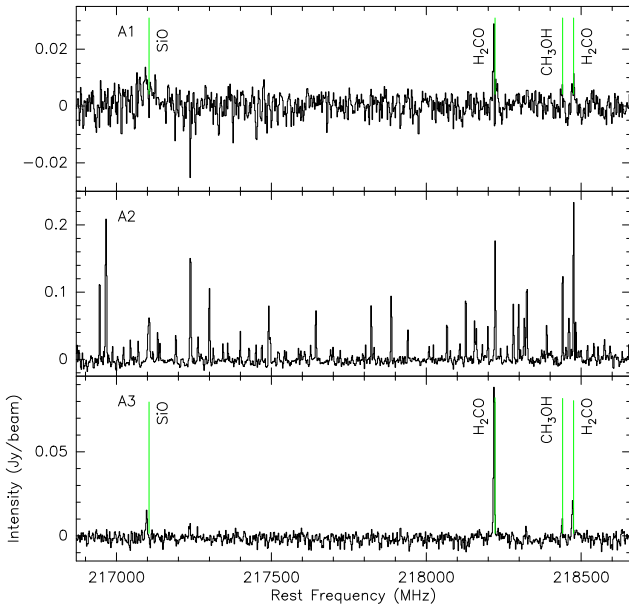
#### 3.1.1. Hot corino at A2

Figure 2 presents the WideX spectra observed at the three continuum source positions. A chemically rich spectrum is detected only towards A2, highlighting a hot-corino chemistry for this

<sup>1</sup> <http://irfu.cea.fr/Projects/Calypso>

<sup>2</sup> <http://www.iram.fr/IRAMFR/GILDAS/>

protostar. As already shown by Taquet et al. (2015), emission from several COMs is indeed observed at A2, such as  $\text{CH}_3\text{OH}$  (methanol),  $\text{HCOOH}$  (formic acid),  $\text{CH}_3\text{OCHO}$  (methyl formate), and  $\text{CH}_3\text{OCH}_3$  (dimethyl ether); similar molecules are observed towards the Class 0 protostar IRAS2A (Maury et al. 2014). A detailed identification and analysis of the detected lines will be presented in a forthcoming paper. For the scope of this paper, this emission is indicative of a rich hot-corino chemistry associated with source A2. On the other hand, only  $\text{SiO}$ ,  $\text{H}_2\text{CO}$ , and  $\text{CH}_3\text{OH}$  are clearly detected towards the continuum sources A1 and A3.



**Fig. 2.** WideX spectra at 1.4 mm at the position of A1 (upper panel), A2 (middle panel), and A3 (lower panel). We note the typical hot-corino chemically rich spectrum observed towards A2. As already shown by Taquet et al. (2015), the spectrum presents emission from several COMs, such as  $\text{CH}_3\text{OH}$  (methanol),  $\text{HCOOH}$  (formic acid),  $\text{CH}_3\text{OCHO}$  (methyl formate), and  $\text{CH}_3\text{OCH}_3$  (dimethyl ether).

### 3.1.2. Infall signatures

Figure 3 presents the high-resolution spectra at the continuum source positions of the selected molecular species. Absorption is detected towards A1 and A2 in  $^{12}\text{CO}$ ,  $^{13}\text{CO}$ , and  $\text{SO}$  at similar slightly red-shifted velocities ( $\sim 8.2 \text{ km s}^{-1}$ ). In particular, the  $^{13}\text{CO}$  spectra show inverse P-Cygni profiles, which are indicative of infall motions. Similar profiles were previously detected in  $\text{H}_2\text{CO}$  and  $\text{CS}$  with PdBI and NRO-NMA by Di Francesco et al. (2001). The authors modelled the emission with a two-layer radiative transfer code and interpreted it as infall in the warm gas associated with the young stellar objects. Inverse P-Cygni profiles were also observed in  $^{13}\text{CO}$  with the SMA by Jørgensen et al. (2007) and interpreted as larger scale infall motions in the ambient cloud or outer envelope rather than collapse onto the central protostars. For the first time, we spatially resolve the absorption and detect infall signatures associated with both known protostars A1 and A2 at similar velocity. Whether the detected spectra presented here probe infall towards each source or global infall of a common envelope is not clear from our data and a detailed modelling of the line profiles is certainly needed in order to resolve this issue. However, this is beyond the scope of this paper. We note that infall motions on larger scales associated with

the envelope of IRAS4A were observed in  $\text{HCN}$  by Choi et al. (1999) and in  $\text{CS}$ ,  $\text{C}^{34}\text{S}$ , and  $\text{N}_2\text{H}^+$  by Belloche et al. (2006).

Interestingly, red-shifted absorption is also detected in  $^{12}\text{CO}$  and  $^{13}\text{CO}$  towards the newly detected continuum source A3.

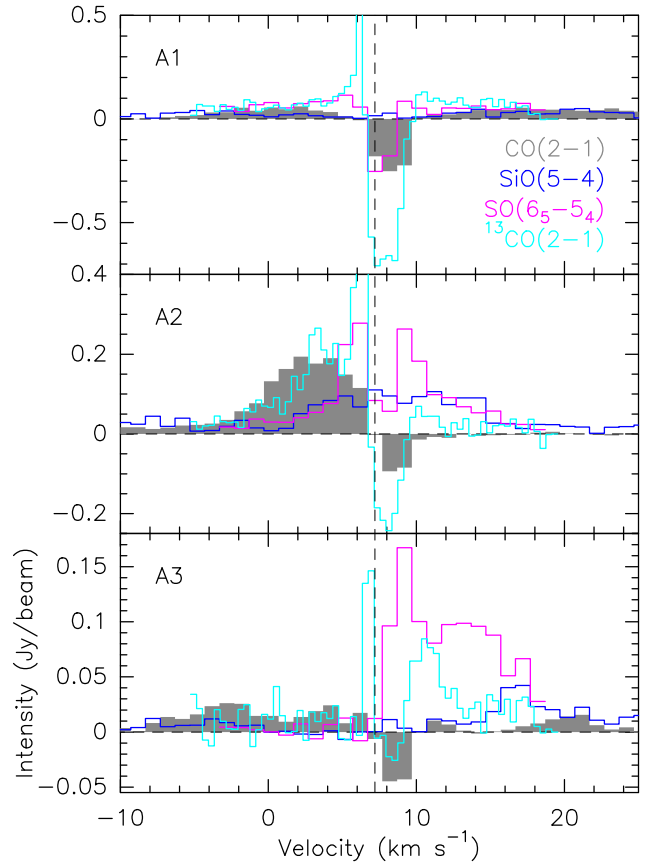


**Fig. 3.**  $^{12}\text{CO}(2-1)$  (grey),  $\text{SiO}(5-4)$  (blue),  $\text{SO}(6_5-5_4)$  (magenta), and  $^{13}\text{CO}(2-1)$  (cyan) at the positions of the continuum sources A1, A2, and A3 (see Fig. 5). The selected positions are displayed from top to bottom. The  $^{12}\text{CO}(2-1)$  data have been convolved to match the angular resolution at 1.4 mm ( $1''.1 \times 0''.8$ ). The vertical dashed line marks the systemic velocity of  $+7.2 \text{ km s}^{-1}$  for the three continuum sources. We note that the systemic velocity of A3 has been derived from PdBI  $\text{N}_2\text{H}^+(1-0)$  observations at 93.17 GHz from our CALYPSO dataset.

### 3.2. Line emission: jet multiplicity

Figure 4 shows the velocity-integrated emission of  $\text{SiO}(5-4)$ ,  $\text{SO}(6_5-5_4)$ , and  $^{12}\text{CO}(2-1)$  towards IRAS4A, in comparison with the *Spitzer*-IRAC map of band 2 at  $4.5 \mu\text{m}$ . This IRAC band covers several  $\text{H}_2$  emission lines, which are particularly strong in shocked regions making IRAC images good tracers of  $\text{H}_2$  emission (e.g. Reach et al. 2006; Neufeld & Yuan 2008). For the first time the bipolar outflow is clearly disentangled in the southern blue-shifted emission into two different flows tracing the jets driven by the A1 and A2 protostars.  $\text{SiO}$  emission is detected for the first time in IRAS4A at close distance from the continuum sources, inside  $\sim 10''$  ( $\sim 2400 \text{ AU}$ , see Choi 2005; Choi et al. 2006). Strong IRAC  $\text{H}_2$  emission is only associated with the jet from A1, which possibly indicates a stronger shock or the presence of denser ambient material. In particular, the bright southern and northern  $\text{H}_2$  knots in the IRAC map coincide with the tips of the blue-shifted and red-shifted (see also Fig. 5) A1 lobes seen in our  $\text{SiO}$  map. Since there is no  $\text{H}_2$  or single-dish  $\text{CO}$  outflow signature further along the A1 jet axis, as can be seen on

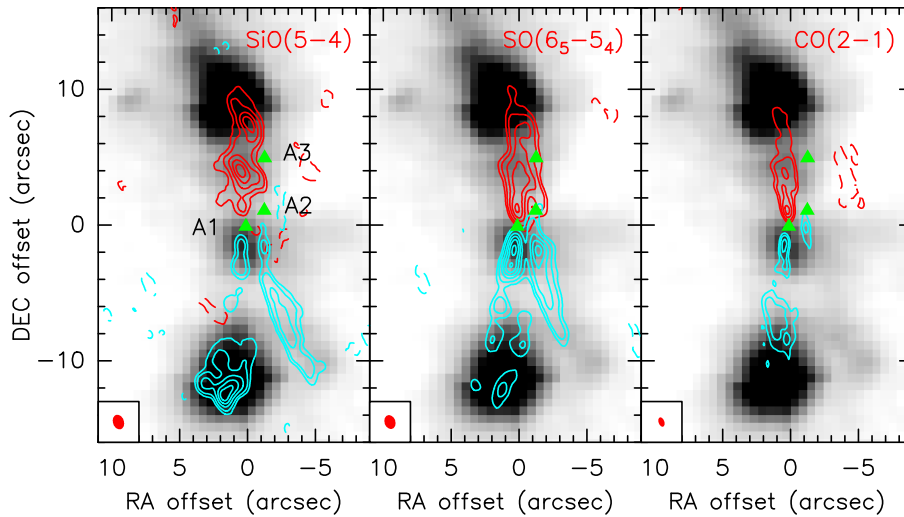


**Fig. 4.** *Left:* The *Spitzer*-IRAC map of band 2 at  $4.5\ \mu\text{m}$  (grey scale) is compared with the SiO(5–4) map integrated in the blue- ( $-20, +5\ \text{km s}^{-1}$ , cyan contours) and red-shifted ( $+10, +55\ \text{km s}^{-1}$ , red contours) velocity ranges. Offsets are with respect to IRAS4A1. The contour levels of emission are traced at  $5$  and  $8\ \sigma$  levels and increase in steps of  $5\ \sigma$ , where  $\sigma=100\ \text{mJy beam}^{-1}$  for the red-shifted emission and  $70\ \text{mJy beam}^{-1}$  for the blue-shifted emission. Negative emission is shown with dashed contours starting at the  $3\ \sigma$  level and decreasing in steps of  $3\ \sigma$ . The positions of the continuum sources at  $1.3\ \text{mm}$  are marked in green. The PdBI synthesised beam (HPBW) is shown in the bottom-left corner. *Middle and Right:* Same as the left panel for the SO( $6_5-5_4$ ) and  $^{12}\text{CO}(2-1)$  emissions, respectively. The rms noise of the velocity-integrated maps are:  $\sigma=110\ \text{mJy beam}^{-1}$  and  $90\ \text{mJy beam}^{-1}$  for the red- and blue-shifted SO( $6_5-5_4$ ) emissions, respectively; and  $\sigma=500\ \text{mJy beam}^{-1}$  and  $400\ \text{mJy beam}^{-1}$  for the red- and blue-shifted  $^{12}\text{CO}(2-1)$  emissions, respectively.

larger scales from the IRAC and APEX maps in Santangelo et al. (2014), it appears that here we are tracing the terminal shocks, where the A1 outflow impacts the ambient cloud. Remarkably, our observations detect a sharp bend to the south-west of the blue-shifted A2 jet at a distance of about  $4''$  from the driving source. On the other hand, emission from the two sources cannot be disentangled in the velocity-integrated SiO red-shifted northern emission, possibly because geometric effects cause mixing of the emission; possible additional confusion may be due to the presence of the continuum source A3.

The two jets are also unraveled in the SO emission. The SO morphology is different with respect to SiO, with the latter peaking at the tip of the blue-shifted lobe of the A1 outflow, in association with the IRAC  $\text{H}_2$  emission, and clearly delineating the A2 jet over more than  $10''$  all the way down to the source, whereas the SO emission peaks closer to the protostars. Finally, in the CO emission only the A1 jet is clearly detected; the strongest peak of the blue-shifted lobe appears to be shifted with respect to the IRAC  $\text{H}_2$  and SiO emissions, further suggesting a chemical differentiation in the jet. Faint and compact blue-shifted CO emission associated with the A2 jet is only detected close to the driving source, before the bend.

### 3.3. Line emission: jet kinematics

A more detailed view of the region, showing in particular the multiplicity and differentiation of the A1 and A2 jets, is given by the channel maps of the molecular emission presented in Fig. 5. Four velocity ranges are identified in CO, SiO, and SO emissions, corresponding to the systemic ( $v_{\text{sys}} \pm 1.5\ \text{km s}^{-1}$ ), low-velocity (LV, from  $v_{\text{sys}} \pm 2.5\ \text{km s}^{-1}$  to  $v_{\text{sys}} \pm 17.5\ \text{km s}^{-1}$ ), high-velocity (HV, from  $v_{\text{sys}} + 18.5\ \text{km s}^{-1}$  to  $v_{\text{sys}} + 32.5\ \text{km s}^{-1}$  and from  $v_{\text{sys}} - 18.5\ \text{km s}^{-1}$  to  $v_{\text{sys}} - 27.5\ \text{km s}^{-1}$ ), and extremely high-velocity (EHV, from  $v_{\text{sys}} + 33.5\ \text{km s}^{-1}$  to  $v_{\text{sys}} + 47.5\ \text{km s}^{-1}$ ) gas. Compact and spatially unresolved absorption is detected around systemic velocity ( $v_{\text{sys}} = +7.2\ \text{km s}^{-1}$ , Belloche et al. 2006) to-

wards A1, A2, and A3 in CO emission and only towards A1 in SO, as already shown in Sect. 3.1.2. An extended structure with A2 at the vertex is seen in SO emission at the systemic velocity, possibly probing the hot corino and outflow cavity walls (see also Sect. 3.1.1 and Codella et al. 2014, for NGC1333-IRAS2A).

The molecular emissions integrated over the higher velocity channels show that we are finally able to disentangle both the blue- and red-shifted outflow emissions associated with the two protostars A1 and A2. In particular, we resolve the red-shifted counterpart of the A1 southern outflow for the first time. The A1 jet appears to be faster than the A2 jet as shown by its association with HV and EHV emissions; in particular, jet-like gas at red-shifted EHV is detected in association with the A1 jet, showing a strong compact peak about  $4''$  north with respect to A1. On the other hand, the A2 jet is brightest in the LV range, with only faint molecular line emission in the HV range. The sharp bend of the A2 jet observed at these small scales in the velocity-integrated blue-shifted SiO and SO emissions (see previous section) is detected in the LV and HV channel maps. They also clearly show a symmetric bending in the northern red-shifted A2 jet emission at about  $4''$  from A2, which is close to the continuum source A3. The symmetric morphology of the bend suggests a jet precession on very short timescales. Indeed, assuming an observed velocity of  $10\text{--}20\ \text{km s}^{-1}$  (see Fig. 3) and an inclination with respect to the line of sight of about  $45^\circ\text{--}60^\circ$  (see Yıldız et al. 2012), the dynamical age of the bend is about  $200\text{--}600\ \text{yr}$ . After this bending, the axes of the A2 jet correspond to the axes of the large-scale SiO and CO outflow emissions (see e.g. Blake et al. 1995; Girart et al. 1999; Choi 2001, 2005, and Fig. A.1 in Appendix A), confirming that the large-scale outflow emission is driven by the A2 protostar. In this context, the non-detection of CO(2–1) emission associated with the A2 jet at distance larger than  $\sim 3''$  even in the LV range may be due to the filtering out of extended emission by the interferometer, given the high angular resolution at  $1.3\ \text{mm}$ .



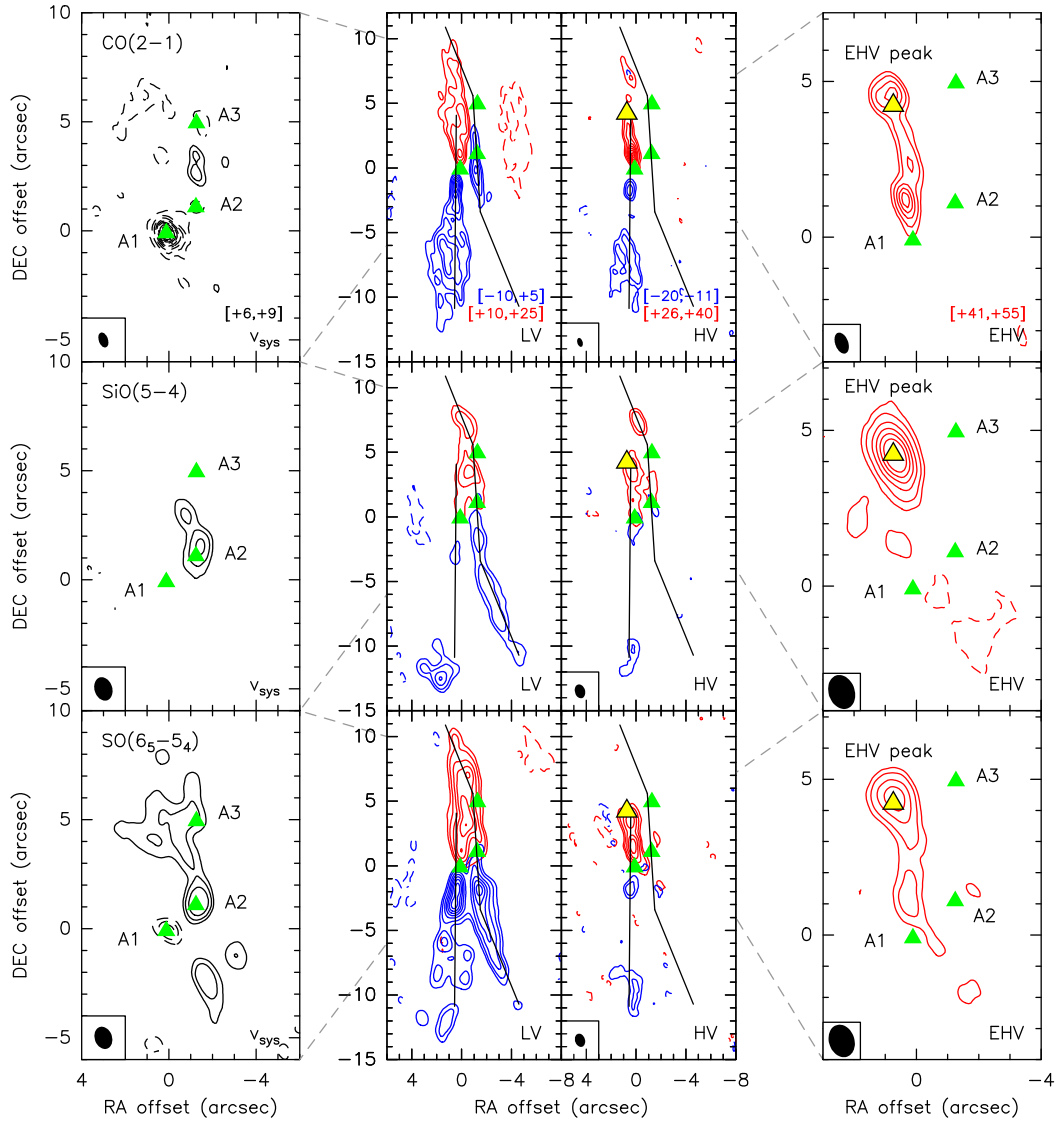


**Fig. 5.** *Upper:* Channel maps of the  $^{12}\text{CO}(2-1)$  emission integrated in the ambient systemic- ( $v_{\text{sys}}$ ; +6, +9  $\text{km s}^{-1}$ ), low- (LV; -10, +5  $\text{km s}^{-1}$  and +10, +25  $\text{km s}^{-1}$ ), high- (HV; -20, -11  $\text{km s}^{-1}$  and +26, +40  $\text{km s}^{-1}$ ), and extremely high- (EHV, +41, +55  $\text{km s}^{-1}$ ) velocity ranges. The contour levels of emission are traced at 5 and 8  $\sigma$  levels and increase in steps of 5  $\sigma$ . Negative emission is shown with dashed contours starting at the 3  $\sigma$  level and decreasing in steps of 3  $\sigma$ . The positions of the continuum sources at 1.3 mm are marked in green and the position of the SiO(5-4) emission peak in the EHV range is marked in yellow. The PdBI synthesised beams (HPBW) are shown in the bottom-left corner. Solid black curves indicate the proposed propagation directions of the A1 and A2 jets. *Middle:* Same as the upper panel for the SiO(5-4) emission. *Lower:* Same as the upper panel for the SO(6<sub>5</sub>-5<sub>4</sub>) emission.

## 4. Analysis and discussion

### 4.1. Chemical abundances in the A1 jet at the EHV peak

Red-shifted EHV (41–55  $\text{km s}^{-1}$ ) emission is detected in CO, SiO, SO, and  $\text{H}_2\text{CO}$  (see Figs. 5, 6, and B.1). It shows a compact ( $\sim 1''.6 \times 1''.1$  from visibility fitting) morphology in the SiO emission with the emission peak located (+0''.7, +4''.3) offset from A1, whereas a more elongated and collimated structure pointing to A1 is detected in the CO and SO emissions.

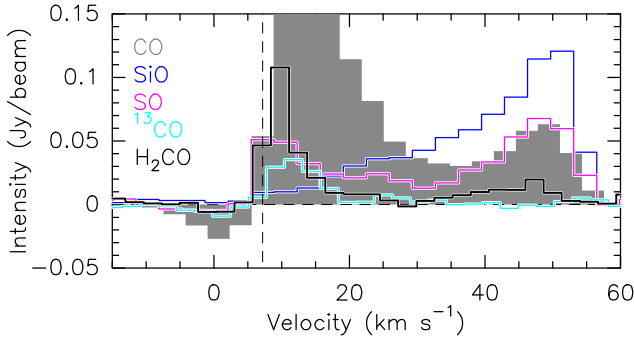
A line profile comparison at the EHV peak reveals that CO, SO, and  $\text{H}_2\text{CO}$  show an emission peak at low velocity ( $\sim 10 \text{ km s}^{-1}$ ) and a secondary EHV peak around +50  $\text{km s}^{-1}$ ; the non-detection of EHV  $^{13}\text{CO}$  is due to a lack of sensitivity (if CO is optically thin, the expected  $^{13}\text{CO}$  at the EHV peak of  $^{12}\text{CO}$  is approximately the same as the rms noise). On the other hand, the SiO line profile presents an emission peak at +50  $\text{km s}^{-1}$  with a wing extending down to the systemic velocity. We note

that this is the first detection of SiO emission at such high velocity in this source (Choi 2005; Choi et al. 2011). The similarity between peak velocities and line profiles of the molecules detected at EHV suggests that they share a common origin, tracing the primary molecular jet (see also Codella et al. 2014).

Abundances of the detected species have been derived under the assumption of LTE conditions, using CO as a proxy for  $\text{H}_2$  emission. The emission has been divided into two velocity ranges: LV (9–25  $\text{km s}^{-1}$ ) and (E)HV (26–55  $\text{km s}^{-1}$ ). For the analysis, two values of temperature have been considered: 40 and 300 K. Since  $^{12}\text{CO}$  emission is optically thick at velocities close to systemic ( $\tau^{12}\text{CO} \sim 11$ ), we use  $^{13}\text{CO}$  ( $\tau^{13}\text{CO} \sim 0.1$ ) to derive abundances in the LV range, assuming optically thin conditions and  $^{12}\text{C}/^{13}\text{C} = 77$  (Wilson & Rood 1994). On the other hand, abundances in the (E)HV component were obtained using  $^{12}\text{CO}$  ( $\tau^{12}\text{CO} < 14$ ), assuming a typical CO abundance of  $10^{-4}$ . Abundance enhancements are derived for all species in the high-

**Table 2.** Abundances with respect to H<sub>2</sub> of the observed species at 40 and 300 K for the LV and EHV gas.

Mol.	LV (9–25 km s <sup>-1</sup> )					(E)HV (26–55 km s <sup>-1</sup> )				
	T=40 K		T=300 K			T=40 K		T=300 K		
	$\int T dv$ (K km s <sup>-1</sup> )	$N$ (cm <sup>-2</sup> )	$X^a$ (10 <sup>-8</sup> )	$N$ (cm <sup>-2</sup> )	$X^a$ (10 <sup>-8</sup> )	$\int T dv$ (K km s <sup>-1</sup> )	$N$ (cm <sup>-2</sup> )	$X^b$ (10 <sup>-8</sup> )	$N$ (cm <sup>-2</sup> )	$X^b$ (10 <sup>-8</sup> )
<sup>13</sup> CO	8.6	1.2×10 <sup>16</sup>	–	6.4×10 <sup>16</sup>	–	–	–	–	–	–
<sup>12</sup> CO <sup>c</sup>	–	–	–	–	–	31.4	2.0×10 <sup>16</sup>	–	1.1×10 <sup>17</sup>	–
SiO	–	–	–	–	–	61.9	8.3×10 <sup>13</sup>	41	3.2×10 <sup>14</sup>	29
SO	14.4	1.8×10 <sup>14</sup>	1.9	7.3×10 <sup>14</sup>	1.5	28.7	3.5×10 <sup>14</sup>	170	1.5×10 <sup>15</sup>	140
p-H <sub>2</sub> CO	14.6	1.5×10 <sup>14</sup>	1.7	2.1×10 <sup>15</sup>	4.3	5.8	6.2×10 <sup>13</sup>	30	8.5×10 <sup>14</sup>	79

**Notes.** <sup>(a)</sup>  $X(^{12}\text{C}/^{13}\text{C})=77$  (Wilson & Rood 1994). <sup>(b)</sup>  $X(^{12}\text{CO}/\text{H}_2)=10^{-4}$ . <sup>(c)</sup> The <sup>12</sup>CO(2–1) data have been convolved to match the angular resolution at 1.4 mm (1'1×0'8).

**Fig. 6.** <sup>12</sup>CO(2–1) (grey), SiO(5–4) (blue), SO(6<sub>5</sub>–5<sub>4</sub>) (magenta), <sup>13</sup>CO(2–1) (cyan), and p-H<sub>2</sub>CO(3<sub>03</sub>–2<sub>02</sub>) (black) spectra at the EHV peak (see Fig. 5). The p-H<sub>2</sub>CO(3<sub>03</sub>–2<sub>02</sub>) spectrum was observed with WideX (see Appendix B) at the spectral resolution of ~2.7 km s<sup>-1</sup>; all other spectra have thus been smoothed to the same spectral resolution. The <sup>12</sup>CO(2–1) data have been convolved to match the angular resolution at 1.4 mm (1'1×0'8).

velocity gas (Table 2) and suggest a shock origin. In particular, a SiO abundance of  $(2.9\text{--}4.1)\times 10^{-7}$  is derived in the high-velocity gas, consistent with previous single-dish estimates in Class 0 outflows (e.g. Bachiller & Pérez Gutiérrez 1997; Tafalla et al. 2010) and in agreement with current shock model predictions (Gusdorf et al. 2008a,b; Guillet et al. 2009, 2011). However, we note that Cabrit et al. (2012) showed that PdBI SiO(5–4) emission in the HH212 protostellar jet can be optically thick at high velocities and derived an SiO abundance up to about  $3\times 10^{-6}$ .

It has been observed that the SO abundance is enhanced by two orders of magnitude from  $(1.5\text{--}1.9)\times 10^{-8}$  in the low-velocity gas to  $(1.4\text{--}1.7)\times 10^{-6}$  in the high-velocity gas. The derived abundances are slightly higher than the values observed by Bachiller & Pérez Gutiérrez (1997) and Tafalla et al. (2010), i.e.  $\sim (2\text{--}3)\times 10^{-7}$ , although their estimates are based on single-dish observations. On the other hand, an SO abundance of  $2\times 10^{-6}$  is derived by Lee et al. (2010) in the HH211 Class 0 jet from SMA interferometric observations. Pineau des Forets et al. (1993) and Flower & Pineau des Forets (1994) modelled SO emission in C-type shocks and predicted an increase of SO abundance in shock regions with maximum values of a few  $10^{-7}$ , consistent with our estimates.

Finally, an enhancement of the p-H<sub>2</sub>CO abundance from  $(1.7\text{--}4.3)\times 10^{-8}$  to  $(3\text{--}7.9)\times 10^{-7}$  is observed between the low- and high-velocity gas components. This is not in agreement with the estimates for Class 0 outflows by Tafalla et al. (2010), who reported higher abundance values in the low-velocity gas (a few  $10^{-8}$  with respect to  $<10^{-8}$  for the high-velocity gas). Their re-

sults, however, are based on single-dish observations. It is worth noting that this molecule is expected to be released from icy mantles, which would support our detection of an abundance increase in fast shocks. Given the size of the beam, the estimated H<sub>2</sub>CO abundances are in agreement with C-type shock models including grain-grain processing, as described in Anderl et al. (2013).

#### 4.2. Different properties of the A1 and A2 jets

The new PdBI data presented in this paper highlight the intrinsic differences between the jets driven by the two protostars A1 and A2. In particular, the jets present different morphologies with the A2 jet bending on small scales in a mirror-symmetric S-shaped pattern, while the A1 jet is C-shaped with the blue- and red-shifted emissions both tilted to the east of A1. The A1 jet appears to be faster than the A2 jet, as can be seen from its association with bright HV and EHV emissions, whereas the A2 jet is mainly detected in the LV range. Finally, the A2 jet shows a large spatial extent on the sky of more than 4', while the A1 jet is only about 20'' long. Three possible explanations may be invoked in order to account for the different observational characteristics of the jets associated with the two protostars: 1) different inclinations for the jets, 2) different masses for the driving sources, or 3) different ages for jets and driving sources.

A jet inclination effect could explain the large difference in projected lengths for the two outflows. In this case, assuming the same intrinsic length for both jets (about 120'' for each lobe), the projected length of the A1 jet (about 13'' in the blue-shifted lobe) suggests that it should be viewed at about 6° from pole-on. This is, however, statistically very unlikely and not consistent with the morphology of the emission we observed (see Cabrit & Bertout 1986, 1990, for a review).

In the second case, since it is expected that more massive objects drive faster jets<sup>3</sup>, we would expect A1 to be more massive than A2. Indeed, A1 represents the source driving the faster jet. Moreover, the detection of brighter continuum emission associated with A1 (see Sect. 3.1) may be interpreted as a larger envelope mass and, hence perhaps, larger protostellar mass. However, this scenario is not supported by our WideX spectra at the positions of the detected continuum sources (see Fig. 2). In fact, a chemically rich spectrum, with emission from several COMs, is detected only towards A2, highlighting a hot-corino chemistry for this protostar.

<sup>3</sup> The outflow velocity is related to the escape speed of the driving object, thus it increases as the square root of the mass of the central object (e.g. Banerjee & Pudritz 2006).

In the third case, A1 is expected to be younger than A2, as already suggested by Choi et al. (2007, 2010, 2011) based on the disks and outflows properties from VLA  $\text{NH}_3$  and  $\text{SiO}$  observations. This view is supported by the detection of a hot-corino chemistry only towards A2 (see Sect. 3.1.1 and Fig. 2). Along with a slower jet driven by A2, associated with weaker  $\text{H}_2$  shocked emission, a different chemistry may indicate a later evolutionary stage for this source. Indeed the lack of a detectable hot corino at A1 suggests a lower internal luminosity than at A2; in particular, the region where the dust temperature is high enough ( $\geq 100$  K) for the icy mantles to sublimate should be much smaller and more heavily beam diluted than at A2. This would imply a smaller stellar mass and/or earlier evolutionary stage for A1. Further support for this view is given by the short dynamical timescale of the A1 jet. In fact, for the farthest  $\text{SiO}$  knot along the A1 jet, assuming an observed velocity of  $10\text{--}20\text{ km s}^{-1}$  (see Fig. 3), we can estimate a dynamical age of  $\lesssim 10^3$  yr. The A1 jet indeed appears as an intrinsically very young outflow. On the other hand, according to Awad et al. (2010), the chemically rich emission detected at A2 suggests an age of  $\gtrsim 10^4\text{--}10^5$  yr for this source, which is in agreement with the collapse age of  $5 \times 10^4$  yr derived by Choi et al. (2010) from the rotation kinematics of the disk in  $\text{NH}_3$ .

## 5. Summary and conclusions

Our new PdBI observations of the IRAS4A binary system finally allowed us to clearly disentangle the jet emission from the Class 0 driving protostars, revealing the intrinsic different properties of the two jets. The detection of such a tight and collimated protobinary system is challenging for current theoretical models of multiple system formation. We propose that the observed properties of the jets can be explained with different evolutionary stages for the two driving protostars. In particular, the younger source (A1) drives a fast collimated jet associated with bright  $\text{H}_2$  emission, whereas its sibling protostar (A2) powers a slower precessing jet and is associated with a rich hot-corino chemistry. However, a difference in the protostellar masses may not be excluded with certainty. Indeed, information on the individual luminosities of the protostars would be crucial in order to confirm the proposed scenario. Finally, jet variability, in particular episodic ejection (see e.g. Codella et al. 2014), may also play a role.

**Acknowledgements.** We thank Serena Viti and Brunella Nisini for fruitful discussions and helpful inputs on this project. We are very grateful to the IRAM staff, whose dedication allowed us to carry out the CALYPSO project. This work was partly supported by the ASI-INAF project 01/005/11/0, the PRIN INAF 2012 – JEDI, and the Italian Ministero dell’Istruzione, Università e Ricerca through the grant Progetti Premiali 2012 – iALMA.

## References

Anderl, S., Guillet, V., Pineau des Forêts, G., & Flower, D. R. 2013, *A&A*, 556, A69  
 André, P., Ward-Thompson, D., & Barsony, M. 2000, *Protostars and Planets IV*, 59  
 Arce, H. G., Shepherd, D., Gueth, F., et al. 2007, *Protostars and Planets V*, 245  
 Awad, Z., Viti, S., Collings, M. P., & Williams, D. A. 2010, *MNRAS*, 407, 2511  
 Bachiller, R., & Pérez Gutiérrez, M. 1997, *ApJ*, 487, L93  
 Banerjee, R., & Pudritz, R. E. 2006, *ApJ*, 641, 949  
 Belloche, A., Hennebelle, P., & André, P. 2006, *A&A*, 453, 145  
 Blake, G. A., Sandell, G., van Dishoeck, E. F., et al. 1995, *ApJ*, 441, 689  
 Bottinelli, S., Ceccarelli, C., Lefloch, B., et al. 2004, *ApJ*, 615, 354  
 Cabrit, S., & Bertout, C. 1986, *ApJ*, 307, 313  
 Cabrit, S., & Bertout, C. 1990, *ApJ*, 348, 530  
 Cabrit, S., Codella, C., Gueth, F., & Gusdorf, A. 2012, *A&A*, 548, LL2  
 Ceccarelli, C. 2004, *Star Formation in the Interstellar Medium: In Honor of David Hollenbach*, 323, 195

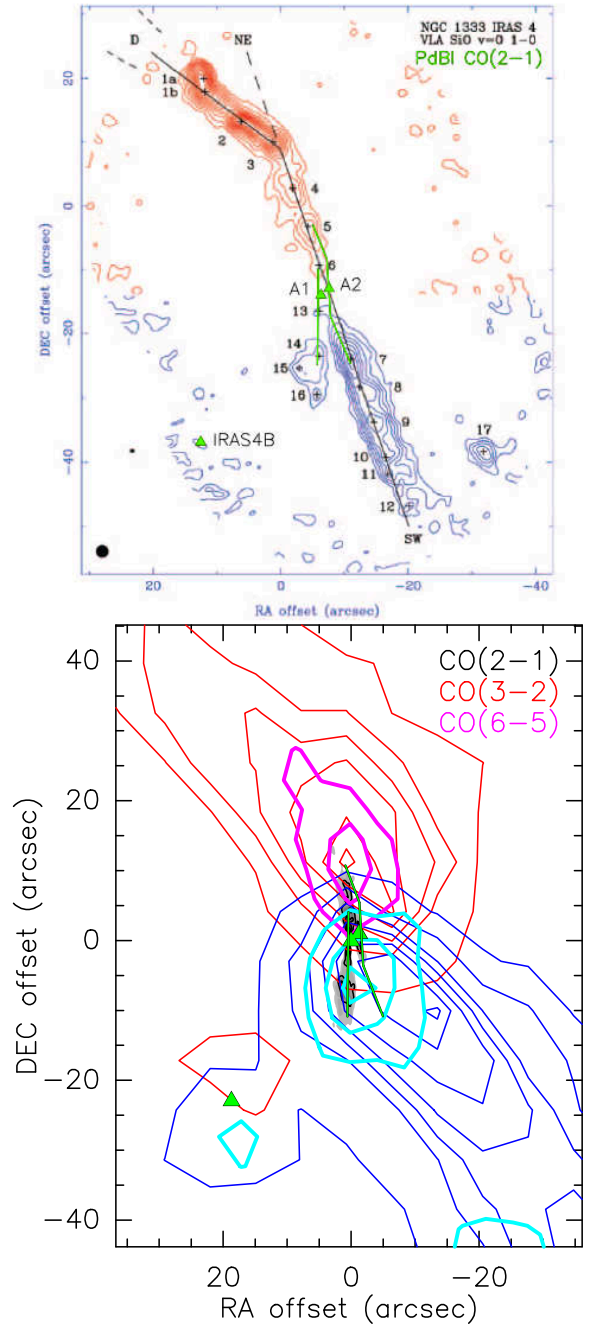
Choi, M., Panis, J.-F., & Evans, N. J., II 1999, *ApJS*, 122, 519  
 Choi, M. 2001, *ApJ*, 553, 219  
 Choi, M. 2005, *ApJ*, 630, 976  
 Choi, M., Hodapp, K. W., Hayashi, M., et al. 2006, *ApJ*, 646, 1050  
 Choi, M., Tatematsu, K., Park, G., & Kang, M. 2007, *ApJ*, 667, L183  
 Choi, M., Tatematsu, K., & Kang, M. 2010, *ApJ*, 723, L34  
 Choi, M., Kang, M., Tatematsu, K., Lee, J.-E., & Park, G. 2011, *PASJ*, 63, 1281  
 Codella, C., Maury, A. J., Gueth, F., et al. 2014, *A&A*, 563, L3  
 Di Francesco, J., Myers, P. C., Wilner, D. J., Ohashi, N., & Mardones, D. 2001, *ApJ*, 562, 770  
 Enoch, M. L., Evans, N. J., II, Sargent, A. I., & Glenn, J. 2009, *ApJ*, 692, 973  
 Evans, N. J., II, Dunham, M. M., Jørgensen, J. K., et al. 2009, *ApJS*, 181, 321  
 Flower, D. R., & Pineau des Forêts, G. 1994, *MNRAS*, 268, 724  
 Frank, A., Ray, T. P., Cabrit, S., et al. 2014, *Protostars and Planets VI*, 451  
 Girart, J. M., Crutcher, R. M., & Rao, R. 1999, *ApJ*, 525, L109  
 Gueth, F., Bachiller, R., & Tafalla, M. 2003, *A&A*, 401, L5  
 Guillet, V., Jones, A. P., & Pineau Des Forêts, G. 2009, *A&A*, 497, 145  
 Guillet, V., Pineau Des Forêts, G., & Jones, A. P. 2011, *A&A*, 527, AA123  
 Gusdorf, A., Cabrit, S., Flower, D. R., & Pineau Des Forêts, G. 2008a, *A&A*, 482, 809  
 Gusdorf, A., Pineau Des Forêts, G., Cabrit, S., & Flower, D. R. 2008b, *A&A*, 490, 695  
 Hirota, T., Bushimata, T., Choi, Y. K., et al. 2008, *PASJ*, 60, 37  
 Jennings, R. E., Cameron, D. H. M., Cudlip, W., & Hirst, C. J. 1987, *MNRAS*, 226, 461  
 Jørgensen, J. K., Bourke, T. L., Myers, P. C., et al. 2007, *ApJ*, 659, 479  
 Karska, A., Herczeg, G. J., van Dishoeck, E. F., et al. 2013, *A&A*, 552, AA141  
 Kristensen, L. E., van Dishoeck, E. F., Bergin, E. A., et al. 2012, *A&A*, 542, A8  
 Lay, O. P., Carlstrom, J. E., & Hills, R. E. 1995, *ApJ*, 452, L73  
 Lee, C.-F., Hasegawa, T. I., Hirano, N., et al. 2010, *ApJ*, 713, 731  
 Looney, L. W., Mundy, L. G., & Welch, W. J. 2000, *ApJ*, 529, 477  
 Maret, S., Ceccarelli, C., Caux, E., et al. 2004, *A&A*, 416, 577  
 Maury, A. J., André, P., Hennebelle, P., et al. 2010, *A&A*, 512, AA40  
 Maury, A. J., Belloche, A., André, P., et al. 2014, *A&A*, 563, L2  
 Neufeld, D. A., & Yuan, Y. 2008, *ApJ*, 678, 974  
 Pineau des Forêts, G., Roueff, E., Schilke, P., & Flower, D. R. 1993, *MNRAS*, 262, 915  
 Ray, T., Dougados, C., Bacciotti, F., Eisloffel, J., & Chrysostomou, A. 2007, *Protostars and Planets V*, 231  
 Reach, W. T., Rho, J., Tappe, A., et al. 2006, *AJ*, 131, 1479  
 Reipurth, B., Rodríguez, L. F., Anglada, G., & Bally, J. 2002, *AJ*, 124, 1045  
 Reipurth, B., Clarke, C. J., Boss, A. P., et al. 2014, *Protostars and Planets VI*, 267  
 Sandell, G., Aspin, C., Duncan, W. D., Russell, A. P. G., & Robson, E. I. 1991, *ApJ*, 376, L17  
 Santangelo, G., Nisini, B., Codella, C., et al. 2014, *A&A*, 568, AA125  
 Tafalla, M., Santiago-García, J., Hacar, A., & Bachiller, R. 2010, *A&A*, 522, AA91  
 Taquet, V., López-Sepulcre, A., Ceccarelli, C., et al. 2015, *arXiv:1502.06427*  
 Tohline, J. E. 2002, *ARA&A*, 40, 349  
 van Dishoeck, E. F., & Blake, G. A. 1998, *ARA&A*, 36, 317  
 Viti, S., Collings, M. P., Dever, J. W., McCoustra, M. R. S., & Williams, D. A. 2004, *MNRAS*, 354, 1141  
 Wilson, T. L., & Rood, R. 1994, *ARA&A*, 32, 191  
 Yıldız, U. A., Kristensen, L. E., van Dishoeck, E. F., et al. 2012, *A&A*, 542, A86

## Appendix A: Comparison with large-scale emission

In this section, a comparison between the IRAM-PdBI CO(2–1) data presented in this paper and the large-scale emission is presented. In particular, VLA SiO emission data from Choi (2005) and single-dish CO data by Yıldız et al. (2012) are shown. The comparison shows the change of propagation direction from north-south to about  $45^\circ$  in the large-scale CO emission (see also Blake et al. 1995; Girart et al. 1999; Choi 2001, 2005), which also seems to be consistent with the large-scale SiO data. Our possible evidence of precession in the A2 jet on very small scales (Fig. 5) is consistent with the large-scale CO and SiO morphologies, confirming that the A2 jet dominates the large-scale emission. Moreover, the non-detection in the IRAM-PdBI data of CO(2–1) emission associated with the A2 jet at distances larger than about  $3''$  from the source is possibly due to filtering of large-scale emission by the interferometer, suggesting that the CO emission associated with the A2 jet is quite extended.

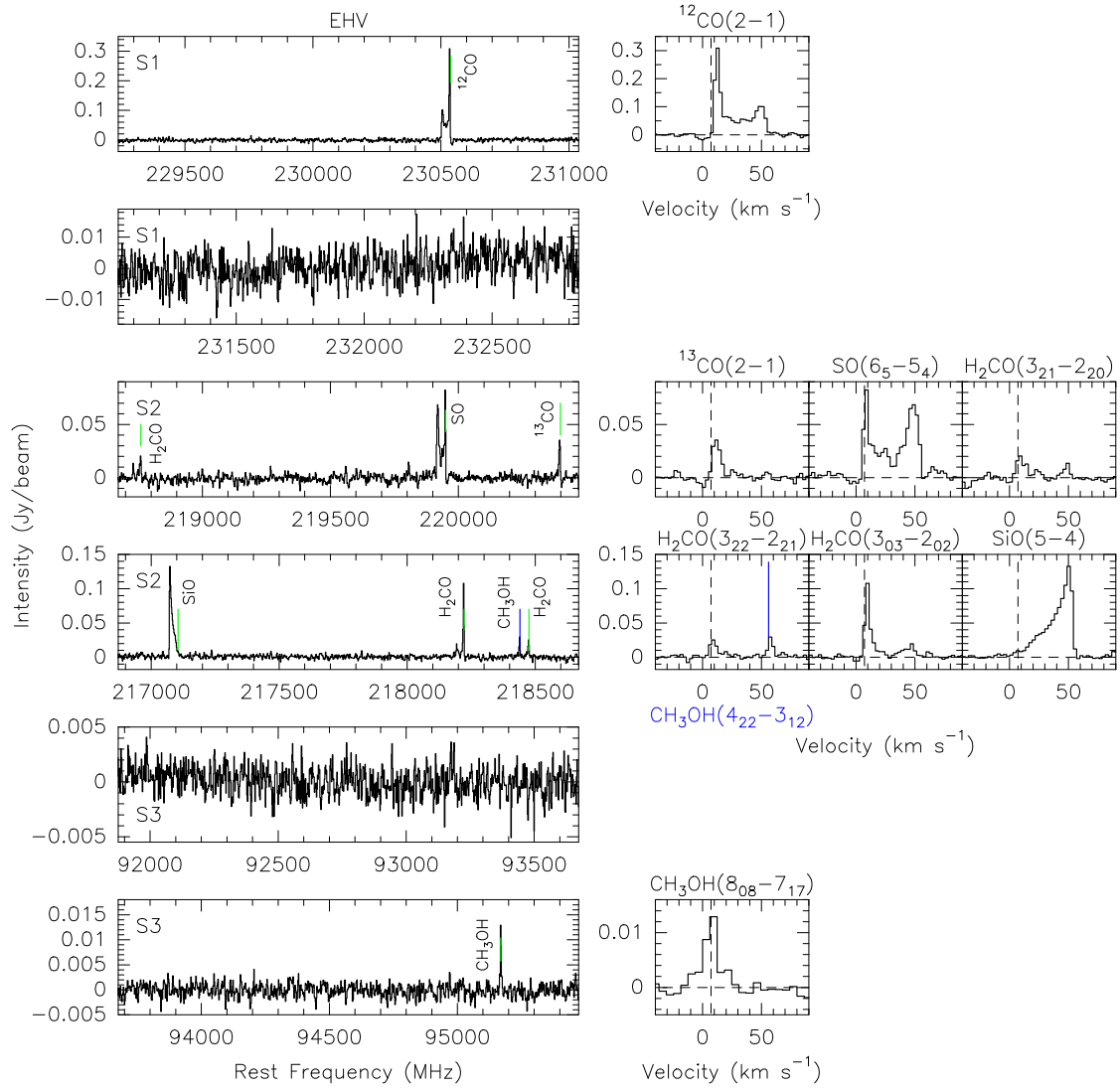
## Appendix B: WideX spectra at the EHV peak

Figure B.1 shows the additional lines detected in the WideX spectra at the peak of the EHV gas that are analysed and discussed in the main text (see also Fig. 6 and Sect. 4.1). In particular, the CO(2–1), SO(6<sub>5</sub>–5<sub>4</sub>), H<sub>2</sub>CO(3<sub>21</sub>–2<sub>20</sub>), and H<sub>2</sub>CO(3<sub>03</sub>–2<sub>02</sub>) lines show a double-peaked profile with a velocity component peaking around the systemic velocity and a secondary velocity component around  $50 \text{ km s}^{-1}$ ; the SiO(5–4) line profile presents a broad wing emission that peaks at  $50 \text{ km s}^{-1}$  and extends down to the systemic velocity; finally, the <sup>13</sup>CO(2–1), H<sub>2</sub>CO(3<sub>22</sub>–2<sub>21</sub>), CH<sub>3</sub>OH(4<sub>22</sub>–3<sub>12</sub>), and CH<sub>3</sub>OH(8<sub>08</sub>–7<sub>17</sub>) line profiles show a single emission peak around systemic velocity, possibly due to a lack of sensitivity.



**Fig. A.1.** *Upper:* The VLA SiO(1–0) map (red and blue contours) by Choi (2005) is shown in comparison with the proposed propagation directions of the A1 and A2 jets (green solid lines, see Fig. 5). The positions of IRAS4A1 and A2 (this work) and of IRAS4B (Looney et al. 2000) are marked with green triangles. *Lower:* The PdBI CO(2–1) map (grey scale and black contours) integrated over the whole velocity range of emission ( $-20, +55 \text{ km s}^{-1}$ ) is compared with the JCMT CO(3–2) (red and blue contours) and APEX CO(6–5) (magenta and cyan contours) maps from Yıldız et al. (2012). CO(2–1) emission is only shown within the PdBI field of view of  $20''$  at  $230 \text{ GHz}$ . The CO(3–2) and CO(6–5) maps are integrated in the velocity ranges between  $-20 \text{ km s}^{-1}$  and  $3 \text{ km s}^{-1}$  for the blue-shifted emission and  $12 \text{ km s}^{-1}$  and  $50 \text{ km s}^{-1}$  for the red-shifted emission. The contour levels start at the  $3 \sigma$  level and increase in steps of  $3 \sigma$  for the CO(2–1) emission, from the  $5 \sigma$  level emission in steps of  $10 \sigma$  for the CO(3–2), and from the  $5 \sigma$  level emission in steps of  $5 \sigma$  for the CO(6–5).





**Fig. B.1.** Additional lines detected in the WideX spectra at the peak of the EHV gas.